Comparison of atmospheric mass density models using a new data source: COSMIC satellite ephemerides

Yang Yang[1,2,3,*], Ronald Maj[1,2], Changyong He[4], Robert Norman[1,2,†], Emma Kerr[1,2], Brett Carter[1], Julie Currie[1], Steve Gower[2]

[1]School of Aeronautics and Astronautics, Sun Yat-Sen University, Guangzhou, Guangdong 510000, China
[2]SPACE Research Centre, School of Science, RMIT University, Melbourne, VIC 3001, Australia
[3]Space Environment Research Centre (SERC) Limited, Mount Stromlo Observatory, Canberra, ACT 2611, Australia
[4]ENSG, Institut national de l'information géographique et forestière (IGN), 77455 Marne-la-Vallée, France

Key Points:

- A new empirical atmospheric mass density model has been developed with a focus on the ion contribution.
- A new data source of COSMIC ephemerides has been used to assess the atmospheric mass density performance in orbit prediction, reducing bias.
- The new atmospheric mass density model outperforms all other state-of-the-art models during the solar maximum period.

*Corresponding Author: Yang Yang, yiyinfeixiong@gmail.com
†Corresponding Author: Robert Norman, robert.norman@rmit.edu.au

Abstract

Atmospheric mass density (AMD) plays a vital role in the drag calculation for space objects in low Earth orbit (LEO). Many empirical AMD models have been developed and used for orbit prediction and efforts continue to improve their accuracy in forecasting high-altitude atmospheric conditions. Previous studies have assessed these models at the height of 200 km to 600 km. A new empirical AMD model, dubbed as the SERC model, was developed by accounting for ion contribution based on the International Reference Ionosphere 2016 model, including many more ions that are not accounted for in other AMD models. This new model has been assessed in orbit prediction by using a new data source of COSMIC satellite ephemerides at the height of ∼800 km, where the contribution of ions in the total AMD is more significant. More specifically, two periods of forty days were chosen in 2014–2015 and 2018–2019, representing the solar maximum and minimum periods, respectively, to assess the SERC model and four other state-of-the-art AMD models. Thorough analyses were conducted to compare OP results using different AMD models with precise reference ephemerides of COSMIC satellites and based on various space weather indices. It is indicated that the SERC model outperforms all other AMD models in terms of OP errors during the solar maximum period and yields comparable OP results during the solar minimum period.

1 Introduction

The ubiquitous use of satellite technology in our modern society, such as through global navigation satellite systems (GNSS), weather observations, and telecommunications, means that determining precise orbital information is vital to track and predict the location of these important satellite assets. Without a clear idea of the future orbital position of a space asset, damage and sometimes total loss can result, such as occurred in 2009 when the inactive Cosmos satellite collided with an active Iridium satellite. Atmospheric mass density (AMD) models play an important role in the determination and prediction of orbits of satellites, especially in low Earth orbit (LEO).

AMD models provide a way to estimate the effect of atmospheric drag and therefore account for perturbations to the simple two-body orbital prediction of satellite trajectories. Other factors such as Earths gravitational variation and solar radiation pressure (SRP) play major roles as well, but for altitudes below 1000 km, the drag acceleration can be larger than SRP due to dense atmosphere.

The earliest models developed in the 1960s were based on empirical data of satellite-drag-derived densities. These were used as boundary conditions to which equations for diffusion, heat conduction and other physical processes were introduced to create tables of density values and the earliest model of the upper atmosphere (Nicolet, 1961). This model was then expanded upon in subsequent years and the familiar Jacchia series was introduced (Jacchia, 1965). The Jacchia series has undergone a number of updates over time (Jacchia, 1970, 1971, 1977) and it has also become the basis for new improved AMD models with the most recent and popular example being the Jacchia-Bowman (JB), or JB2008 model (Bowman et al., 2008), which is now the Committee on Space Research's (COSPAR) reference model for atmospheric drag (Bruinsma, 2015).

The ability to run numerical simulations of the global atmosphere based on first-principles physical processes became possible in the 1970's due to improvements in computing power. This enabled the construction of General Circulation Models (GCM), or numerical computer models that could be used to determine atmospheric mass densities of the upper atmosphere. A number of the better known examples include the National Center for Atmospheric Research's (NCAR's) Thermosphere Ionosphere Electrodynamics General Circulation Model (TIE-GCM) (Qian et al., 2014), the Whole Atmosphere Model (WAM) (Akmaev, 2011) and the Thermosphere extension of the Whole Atmosphere Community Climate Model (WACCM-X) (H.-L. Liu et al., 2010). Physics-based

models have advanced to the stage where they can be reliably used in orbit propagation and produce accurate nowcasts. However their limitation on height (about 650 km (Emmert, 2015)) and the fact that the upper atmosphere is a strongly driven system from features such as solar conditions means that an assimilative upper atmosphere AMD forecasting system using physical models does not yet exist (Emmert, 2015). Therefore, empirical models are still widely used in orbit propagation software.

Empirical models are based upon historical measurements or proxies for the atmospheric density at a given time and location. Various data sources of the historical measurements include the orbiting mass spectrometers, incoherent scatter radars, rocket tests, satellite drag measurements, orbiting accelerometers, solar ultraviolet light occultation measurements, and others (Calabia & Jin, 2016; He et al., 2018). These sources are generally used in conjunction with each other to give a better picture of the global density and its temporal-spatial variations.

Over the years new models have been developed to increase accuracy. However, methods to quantify the improvement over existing models continue to proliferate. In the literature, upon the introduction of a new model, this is generally met with a comparison against the existing state-of-the-art models. For example, when the the American Naval Research Laboratory's MSIS (Mass Spectrometer Incoherent Scatter) extended model (dubbed as MSISE00 hereafter) was introduced in Picone et al. (2002), the authors compared the new model against Jacchia70 and their old MSISE90 model, while in Bruinsma (2015) the Drag Temperature Model 2013 (DTM2013) was introduced with a comparison against their previous DTM2009 and the JB2008 models. In both cases, the log of the ratio of observed data to the predictions made by models at the same time/location was used to quantify model accuracy. The ratio provides a way to handle both over- and under-estimates in a similar fashion. Taking the log of the ratio ensures that the orders of magnitude variations in the atmospheric density do not skew the results. However, the data sources used to compare model predictions against are generally the same data used in the construction of the latest model. This gives a bias towards the newer model being introduced.

In general, performance of these empirical AMD models has been evaluated using three different methods: 1) comparison with total density estimates derived from other in-situ measurements/data (He et al., 2018; Panzetta et al., 2019; March et al., 2019), e.g., the thruster activation data in the GOCE mission (Doornbos et al., 2010) and accelerometer data in the CHAMP, GRACE and SWARM missions (H. Liu et al., 2005; Sutton et al., 2007; Doornbos et al., 2010; Siemes et al., 2016; Mehta et al., 2017); 2) assessment in the orbit prediction (OP) process (Emmert, 2015; He et al., 2018); 3) comparison with physical models (Qian & Solomon, 2012), e.g.,TIE-GCM. Among the literature, mainly three state-of-the-art empirical models are assessed, namely MSISE00, JB2008 and DTM2013.

In this work, the performance of these models for a higher orbit of approximately 800 km in the LEO region will be investigated. Additionally, a newly developed AMD model at SPACE Research Centre, RMIT University and the SERC (Space Environment Research Centre, website: `www.serc.org.au`) consortium is also tested here. This model is novel in its incorporation of a range of ion contributions to the total mass density.

The performance of the models is compared using the predictions from orbit propagation software to quantify model accuracy by determining the deviation from the ephemerides of the COSMIC satellites (Fong et al., 2008). These ephemerides have not been used in any existing model (as far as the authors can tell) and provide an unbiased way to test model accuracy of existing AMD models. More importantly, the COSMIC orbit has not been assimilated into any aforementioned empirical AMD models, hence can generate unbiased assessment results for these models.

The rest of the paper is organised as below. The COSMIC mission is briefly introduced in Sec. 2 with geometric information of the satellites and precise orbit and attitude profiles. Sec. 3 revisits the classical orbit dynamics and elaborates the formulation for surface force modelling of aerodynamical drag and solar radiation pressure (SRP). Five AMD models, MSIS90/00, JB2008, DTM2013 and the SERC model, are introduced in Sec. 4 with focus on their principles, solar drivers and other working conditions. Sec. 5 delineates the comparison methodology and OP results are presented and analyzed. The conclusion of this paper is drawn in Sec. 6.

2 Data source

Constellation Observing System for Meteorology, Ionosphere, and Climate (COSMIC) is a joint US - Taiwan space program to provide high-quality radio occultation profiles for meteorologic, ionospheric, climatological and space weather research (Fong et al., 2008). The constellation consists of six identical satellites and the first one was launched into space in 2006. Currently only four of them are fully operational, in a circular orbit with an altitude of approximately 800 km and an inclination of 72°. The COSMIC satellites are shown in Fig. 1a. The precise ephemerides of these satellites can be retrieved from the COSMIC Data Analysis and Archive Center at `https://cdaac-www.cosmic.ucar.edu`. These ephemerides are calculated in the precise orbit determination process using the spaceborne GPS observations (Hwang et al., 2009). It is reported an orbit accuracy of 2 cm to 3 cm was achieved using both the kinematic and dynamic approaches. Attitude state of the satellites and their solar array drive angles are also provided for accurate effective area calculation (see Fig. 1b for the satellite geometry). In this work, the COSMIC ephemerides will be used for assessing the OP performance with various AMD models.

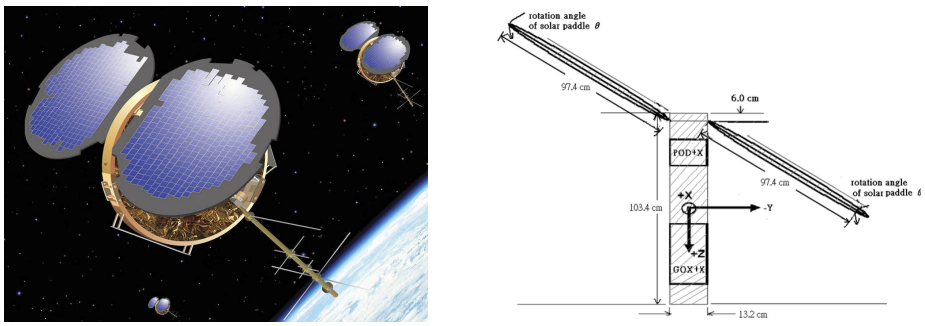

(a) Illustration of COSMIC Satellites (b) Geometry of the COSMIC Satellite

Figure 1: COSMIC Satellite Information (Hwang et al., 2008)

3 Orbit Propagator

For spacecraft in near earth orbit, a Newton-Kepler system is traditionally used to describe the orbit for the two-body case. Real orbit modelling, however, should take into account additional gravitational and non-gravitational perturbations. In general the accelerations acting on the satellite consist of terms for the Earth's geopotential, the third-body gravitational attraction of the sun, moon and other planets, the solar radiation pressure and atmosphere drag on the spacecraft, if no active orbital maneuver is performed. The exact formulations for each term can be obtained from, e.g., Montenbruck & Gill (2000) and Vallado (2001). The dynamic models/parameters used for orbit propagation are summarized in the Table 1.

Table 1: Orbit models used in this paper.

Satellite model	Geometry-based shape
Reference frame	International Celestial Reference Frame
Earth gravity field	GGM05S (100 x 100) model (Ries et al., 2016) Tides corrections (Montenbruck & Gill, 2000)
Third-body attraction	Sun, Moon and planets ephemerides: JPL DE430 (Folkner et al., 2014)
Relativistic effect	Post-Newtonian correction (Montenbruck & Gill, 2000)
Atmospheric drag model	Geometry-dependent projected area Various AMD models
Solar radiation pressure	Geometry-dependent projected area Shadow model: Earth eclipse considered
Numerical integration	Implicit Runge-Kutta solver RADAU II (Hairer & Wanner, 1999)

The motion of the satellite along with the time t is modelled by the conventional orbit dynamics in the Cartesian coordinates:

$$\frac{\mathrm{d}}{\mathrm{d}t}\boldsymbol{x}(t) = \boldsymbol{f}(t, \boldsymbol{x}(t), \boldsymbol{p}(t)) = \begin{pmatrix} \boldsymbol{v}(t) \\ \boldsymbol{a}(t, \boldsymbol{r}(t), \boldsymbol{v}(t)) \end{pmatrix}, \tag{1}$$

where the $\boldsymbol{p}$ is the orbital parameter vector, including the SRP and drag coefficients (C_r and C_d). $\boldsymbol{x}$ comprises the position $\boldsymbol{r}$ and $\boldsymbol{v}$ vectors in the international celestial reference frame. $\boldsymbol{a}$ is the acceleration vector acting on the LEO satellite and can be calculated by modelling the aforementioned perturbative forces. The orbit can be propagated using the integration as follows:

$$\boldsymbol{x}(t) = \boldsymbol{x}(t_0) + \int_{t_0}^{t} \boldsymbol{f}(\boldsymbol{x}, \boldsymbol{p}, t)\mathrm{d}t, \tag{2}$$

where t_0 is the initial epoch.

3.1 Surface forces

A simple canon ball assumption does not represent realistic the shape and geometry of COSMIC satellites. Increased model fidelity can be obtained via summation of the projected areas of different components. Hence the surface forces of drag and SRP can be computed more precisely.

The acceleration due to aerodynamic drag is formulated as (Vallado, 2001):

$$\boldsymbol{a}_{\mathrm{drag}} = -\frac{1}{2} C_d \rho \frac{A_d}{m} |\boldsymbol{v} - \boldsymbol{v}_w| (\boldsymbol{v} - \boldsymbol{v}_w), \tag{3}$$

where ρ is the local atmospheric mass density, A_d is the projected area in the instantaneous direction of travel of the satellite, m is the mass of the satellite, $\boldsymbol{v}$ is the velocity of the space object, and $\boldsymbol{v}_w$ is the velocity of the atmosphere.

The mass of COSMIC before launch was 61.14 kg (Hwang et al., 2008), which can be assumed as a constant throughout the testing days. This value will be used through

out all OP simulations, by neglecting the mass decrease due to the propellant consumption. The COSMIC satellite travels in a manner that the $+X$ direction in Fig. 1 always aligns with the flight direction (Hwang et al., 2008). Hence the total area for surface forces calculation can be formulated as:

$$A_{\text{total}} = A_{\text{main}} + A_{\text{panel}}, \tag{4}$$

with

$$\begin{aligned} A_{\text{main}} &= 1.034 \times 0.132 \ (\text{m}^2), \\ A_{\text{panel}} &= 2 \times \pi \Big(\frac{0.974}{2}\Big)^2 \sin\theta \ (\text{m}^2), \end{aligned} \tag{5}$$

where θ is the rotational angle of the solar panel (see Fig. 1) in and out of the plane, whose thickness is neglected. The projected area for drag calculation is then calculated via:

$$A_d = A_{\text{main}} \operatorname{acos} \frac{\boldsymbol{v} \cdot (\boldsymbol{v} - \boldsymbol{v}_w)}{|\boldsymbol{v}||\boldsymbol{v} - \boldsymbol{v}_w|}. \tag{6}$$

The acceleration due to solar radiation pressure is formulated as (Vallado, 2001):

$$\boldsymbol{a}_{srp} = \gamma C_r \frac{S_f A_s}{m} \Big(\frac{1\,\text{AU}}{R_s}\Big)^2 (\boldsymbol{r} - \boldsymbol{r}_s), \tag{7}$$

where γ is the shadow function with $\gamma = 1$ if the satellite is illuminated by the sun, otherwise $\gamma = 0$. S_f is the solar flux constant; A_s is the projected area for SRP calculation; AU is the astronomical unit; $\boldsymbol{r}_s$ and $\boldsymbol{r}$ are position vector of the Sun and satellite, respectively, and R_s is the satellite-Sun distance. The projected area A_s lies in a plane orthogonal to the vector $(\boldsymbol{r} - \boldsymbol{r}_s)$ and is calculated by assuming that solar panels are always facing the sun and the main body of the satellite is subject to line-of-sight changes of the sun:

$$A_s = A_{\text{main}} \left| \frac{\boldsymbol{v} \cdot (\boldsymbol{r} - \boldsymbol{r}_s)}{|\boldsymbol{v}||\boldsymbol{r} - \boldsymbol{r}_s|} \right| + A_{\text{panel}}. \tag{8}$$

4 Atmospheric Mass Density Models

Precise calculation of the atmospheric drag for orbital perturbation analysis is still challenging due to the uncertainties of the variables in Eq. 3, i.e., the drag coefficient C_d and atmospheric mass density ρ. The uncertainty of the C_d, as well as for the solar radiation pressure coefficient C_r, is quantified using the Monte Carlo simulation in this work. Their mean and standard deviation values can be obtained from the precise orbit determination process (Hwang et al., 2008). Specifically, C_r and C_d vary with a window of 1.5 h. A set of 16 values are generated to cover a whole day as a result and 200 sets of samples are used for each day. Five AMD models will be assessed for their uncertainty analyses by conducting OP.

4.1 Existing Empirical AMD models

The empirical AMD models represent the average climatology of the Earth's atmosphere with parameterized functions such as spherical harmonics and polynomials. Note that it is not appropriate to use the 'resolution' of empirical models since, theoretically, one can calculate density at any location due to the continuous parameterized functions used. Instead, the term 'scale' will be a better alternative. He et al. (2018) investigated that the empirical models have a low horizontal scale of several thousands of kilometers (or 30° to 45°) at the altitudes from 250 km to 800 km.

The most representative empirical models are the MSIS series (Hedin, 1983, 1987; Picone et al., 2002), the DTM series (Bruinsma, 2015) and JB series models (Bowman et al., 2006, 2008). These empirical models are widely used in various space missions due to their computational efficiency.

Table 2: Four existing empirical atmospheric mass density models evaluated.

Model	MSIS90	MSISE00	JB2008	DTM2013
Reference	Hedin (1991)	Picone et al. (2002)	Bowman et al. (2008)	Bruinsma (2015)
Validated altitude	0–2500 km	0–2500 km	175–1000 km	120–1500 km
Time	Local Time	Local Time	Local Solar Time	Local Time
Solar drivers	$F_{10.7}$	$F_{10.7}$	$F_{10.7}$, $S_{10.7}$, $M_{10.7}$ and Y_{10}	F_{30}
Magnetic drivers	a_p	a_p	Dst and a_p	K_m
Compositions	N_2,O_2,Ar He,O,H,N	N_2,O_2,Ar He,O,H,N and anomalous oxygen	N_2, O_2,Ar He,O,H, N	N_2, O_2,He O,H

4.1.1 MSISE90/00

The MSIS series models were first released in 1983 (Hedin, 1983). The MSISE90 is the first MSIS series model which covers the lower atmosphere down to the Earth's surface Hedin (1991). As a follow-on model, MSISE00 represents the atmosphere from the ground to the altitude of 2500 km (Picone et al., 2002). In MSISE90 and MSISE00, spherical harmonic functions are used for the modeling of atmospheric components at a reference height, i.e., N_2, O_2, Ar, He, O, H and N. One particular update of MSISE00 is the modelling of 'anomalous oxygen' (ionized oxygen and hot atomic oxygen) which potentially contributes to the atmospheric drag in the upper thermosphere (Picone et al., 2002). However the anomalous oxygen does not present a significant impact on the orbit prediction at 400 km (He et al., 2018).

The source code of MSISE00 is available at `https://ccmc.gsfc.nasa.gov/modelweb/atmos/nrlmsise00.html`.

4.1.2 JB2008

The JB2008 model was updated from the previous JB2006 model (Bowman et al., 2006). Many new space weather indices were adopted in 2008 for the modelling of thermosphric heating due to ultraviolet radiation and geomagnetic storm. In addition to $F_{10.7}$, i.e., solar flux at the wavelength of 10.7 cm, three new solar parameters are used in JB2008, i.e., $S_{10.7}$, $M_{10.7}$ and Y_{10}, which are respectively the extreme ultraviolet index (26 nm to 34 nm), Mg II index (280 nm), and a weighted index from both the Lyman-α and X-ray indices (see Table 2). Another new geomagnetic index is Dst accounting for the geomagnetic storm effect on the exospheric temperature (Bowman et al., 2008). More description of these indices can be found in the review of He et al. (2018).

This model and required indices are available at `http://sol.spacenvironment.net/jb2008/index.html`.

4.1.3 DTM2013

The DTM2013 model is the latest DTM series model developed in the framework the Advanced Thermosphere Modelling for Orbit Prediction project (ATMOP) (Bruinsma,

2015). DTM2013 and MSISE00 use similar spherical harmonics formulations but with different space weather indices. F_{30} (30 nm) and K_m (based on the a_m index) are used as solar and geomagnetic drivers to DTM2013 for higher fidelity. Note that the F_{30} index used by DTM2013 is scaled to the range of $F_{10.7}$ so that both of these two indices can be used to drive the model.

Due to the ingestion of four-year drag-derived AMD data set from GOCE (Gravity Field and Steady-State Ocean Circulation Explorer) satellite below ~250 km, DTM2013 becomes the most accurate model in the altitude range of 275 km to 170 km compared to MSISE00 and JB2008. DTM2013 is the least biased and most accurate model on all time scales (Bruinsma, Sean et al., 2017).

Since the ATMOP project has been finished, DTM2013 and its required space weather indices are no longer updated. An online run of DTM2013 can be requested at `https://ccmc.gsfc.nasa.gov/requests/IT/DTM/dtm_first.php`.

4.2 New SERC Model

The SERC model was developed with contribution from the SERC consortium. It is, like the other models described thus far, an empirical model that uses a number of variables as input such as the latitude, longitude, altitude of the position of interest as well as the year and day of the year. Fundamentally, the SERC model is composed of two components - neutral and ion contributions that come together to give a overall total atmospheric mass density. The neutrals are modelled based upon the MSISE90 model outputs while the ion contribution is based on the International Reference Ionosphere 2016 (IRI-2016) model, with last update on 02/01/16 (Bilitza et al., 2017). Although at lower altitudes the fraction of mass contributed by ions to the total mass density is quite low, at 800 km it can reach up to 30% (see Fig. 2), which drives the development of the SERC model.

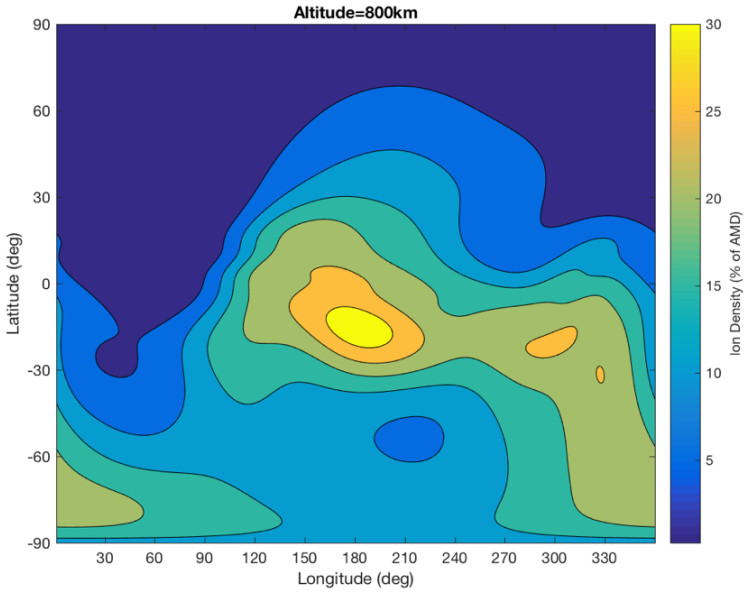

Figure 2: Percentage of ion mass density at an altitude of 800 km, 00:00 universal time and low solar activity. The x axis indicates the longitude in degrees, and the y axis indicates the latitude in degrees. Different colours indicate the values of ion contributions in total atmospheric mass density in percentages.

The IRI ionospheric model has undergone a number of versions since its inception in the 1960s with the tables of IRI-75 giving way to computer-based models from IRI-86 and eventually going online in IRI-95 (Bilitza, 2018). The latest version is the IRI-2016 model. However, even for a given version, there are a number of updates that occur - for example as at the writing of this manuscript, the IRI-2016 model had implemented 24 updates since its release. We have used the 7^{th} update dated 02/01/16 in the SERC model. Updates can be as small as allowing the ability for users to manually choose parameters whereas previously they were automatically determined (such as the B0 and B1 ionospheric parameters introduced in updates 8 and 13) or the introduction of new models for ionospheric values (such as the different hmF2 models described in this paper). These can have small but noticeable differences in the outputs and therefore the version and date of latest update are necessary if IRI results are to be reproduced by readers.

A consideration within the IRI model is the height of the ionospheric F2 layer where the electron density is a maximum (hmF2). The two available models are described in Shubin (2015) and Altadill et al. (2013). The former uses a large dataset of radio occultation measurements from satellite missions CHAMP (2001–2008), GRACE (2007–2011) and COSMIC (2006–2012) as well as ionospheric sounding data from 62 Digisonde ionosondes (1987–2012) while the later uses data from 26 digisonde stations in the Global Ionospheric Radio Observatory (GIRO) network (1998-2006) (Oyekola, 2019). The empirical measurements in both models were used as a basis for predicting the values of hmF2 for different times and locations in the ionosphere - Shubin (2015) determined the median value while Altadill et al. (2013) determined the mean (Oyekola, 2019). The Shubin (2015) predictions for hmF2 were used in the SERC model.

The IRI also has two models available for the critical frequency of the ionosphere's F2 layer (foF2), one developed by the Comité Consultatif International des Radiocommunications (CCIR) (Jones & Obitts, 1970) and the other by the International Union of Radio Science (or URSI after the French acronym for Union Internationale de Radio-Scientifique) Working Group G.5 (Rush et al., 1989). These are based upon averages taken from ionosonde measurements over different times of day and days of the year. The URSI version has been used in the SERC model's implementation.

Therefore, ignoring the contribution of ions, the SERC models would provide the same atmospheric mass density predictions as that of the MSISE90 model. Although the MSISE00 model includes 'anomalous oxygen' as mentioned earlier, other ionic species are not accounted for. The SERC models on the other hand include contributions from all ions modelled under the IRI-2016 model, including H+, He+, O+, O2+, NO+ and N+. This leads to predictions different from both the MSISE90 and MSISE00 models.

5 Comparison Methodology and Results

The aforementioned AMD models were assessed via one-day orbit prediction of the COSMIC satellites. The discrepancy between the COSMIC reference ephemerides and the OP results with each AMD model were calculated in terms of the three dimensional (3D) distance error and component along each direction, especially the in-track direction.

Two data sets of forty day ephemerides were chosen during solar maximum in 2014–2015 and solar minimum in 2018–2019 for COSMIC 1 and COSMIC 6, respectively. We present the data here in 10-day windows distributed in each quarter of the year for each data set (see Fig. 3). Note that the 10-day window may not be consecutive, e.g., Day 275–287, due to unavailable ephemerides or attitude profiles for COSMIC satellites in some days. The average height of each day is also shown in the figure, with values decreasing from 810 km to 806 km during these periods. More specifically, the average height

has a decreasing tendency during 2014–2015 while it stays more fluctuating during 2018–2019. Overall, these height variations with a magnitude of approximately 2 km during each one-year period can be neglected. The reference ephemerides and attitude profiles for the chosen days are provided as the supplemental information.

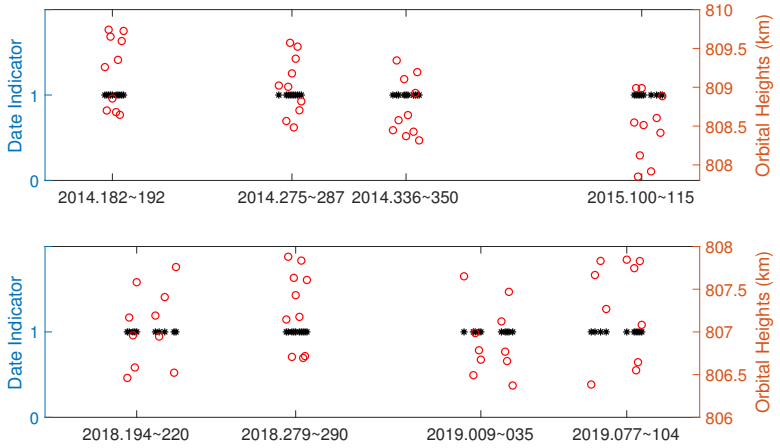

Figure 3: Selected days of COSMIC data and average heights of each day in periods of 2014–2015 and 2018–2019. The top subfigure shows the data in 2014–2015 and the bottom subfigure shows the data in 2018–2019. The black star mark indicates the selected day and the red circle indicates the average orbital height of the COSMIC satellite during the day.

Table 3: Average space weather conditions for each of the 10-day periods investigated.

	F10.7	Ap	X-Ray Flux	# C-Flares	# M-Flares
Solar Max First Ten Days	182	4.9	8.94×10^{-7}	3.3	0.4
Solar Max Second Ten Days	122.6	8.1	2.95×10^{-7}	2.7	0.7
Solar Max Third Ten Days	156	10.4	6.07×10^{-7}	7.7	0.6
Solar Max Fourth Ten Days	137.9	14.6	4.51×10^{-7}	5.3	0.2
Solar Min First Ten Days	70.5	5.2	1.04×10^{-8}	0	0
Solar Min Second Ten Days	70.2	10.3	1.00×10^{-9}	0	0
Solar Min Third Ten Days	71.33	9.5	5.60×10^{-9}	0.2	0
Solar Min Fourth Ten Days	75.6	8.7	1.99×10^{-8}	0.1	0

An important consideration in the variation of the mass density in the upper atmosphere is solar activity. The Sun varies over an approximately 11-year cycle between periods of high and low solar activity (usually referred to as solar maximum and solar minimum). Solar activity is usually quantified by the number of sudden energetic events such as solar flares and coronal mass ejections. Both these events happen as a result of

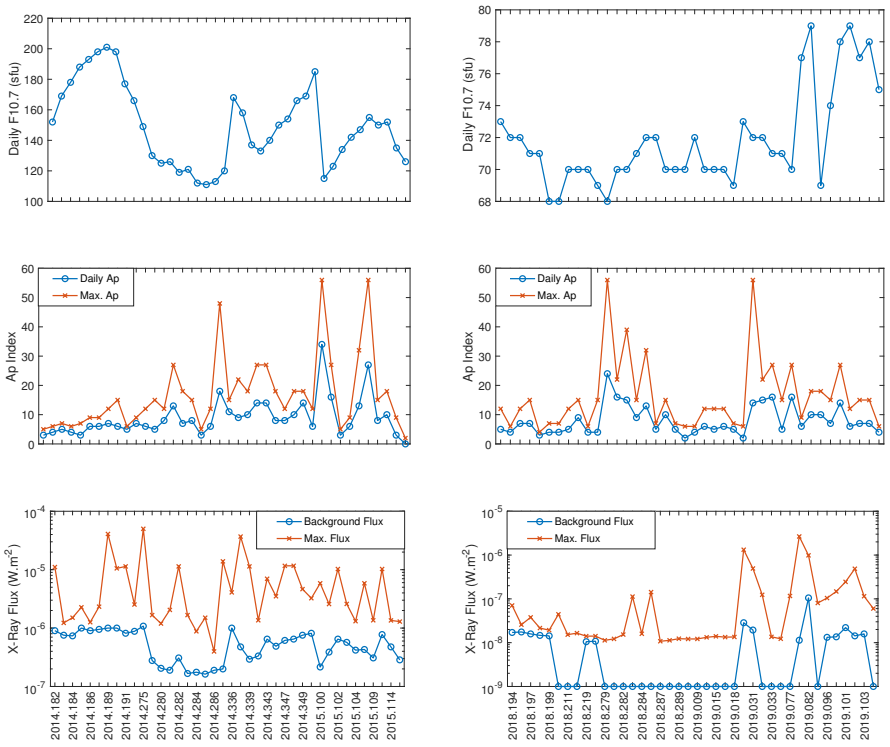

Figure 4: Space weather conditions on the days of the COSMIC ephemerides data sets for solar maximum (left subfigures) and solar minimum (right subfigures). The top subfigures show the F10.7 index in sfu. The middle subfigures show the average (blue circles) and maximum (red crosses) Ap index. The bottom subfigures show the background (blue circles) and the day's maximum X-ray flux (red crosses). Only every second day is labelled on the x axis. Details of data sources are in the acknowledgements.

magnetic reconnection and a conversion of the Sun's surface magnetic energy into light and/or kinetic energy.

The average solar radiation at high frequencies increases during solar maximum periods and therefore produces effects in the upper atmosphere. The highest-frequency radiation such as X-ray, extreme ultraviolet (EUV) and ultraviolet (UV) light contains the largest amount of energy per photon, therefore delivering the greatest amount of energy for a given flux. The amount of energy absorbed by the atmosphere from the Sun leads to variations in its temperature. With increased flux and energy absorption in the upper atmosphere, the atmosphere expands and the atmospheric mass density at a given altitude above the Earth increases. Satellite drag, as a result, has a much larger effect on LEO satellites during solar maximum. This is why data for the COSMIC satellites were chosen for different periods of solar activity (2014–2015 representing solar maximum and 2018–2019 representing solar minimum) and four different periods of the year to reveal the effect of different solar radiation conditions on the atmospheric mass density.

Table 3 and Figure 4 summarize the space weather conditions for the days investigated in the two data sets. The F10.7 averages are of the daily F10.7 values in sfu or solar flux units, Ap are those determined by the Helmholtz Institute in Potsdam and the

X-ray flux values are averages of the background flux values at 1.0 Å to 8.0 Å in $\mathrm{W\,m^{-2}}$ from the GOES-15 satellite (Simões et al., 2015).

The F10.7 index correlates very well with, and is a proxy for, solar UV flux and the number of sunspots. Table 3 and Figure 4 reveal that the F10.7 flux is much higher during solar maximum than solar minimum (approximately double), reflecting well the increased activity of the sun during this period. All the models investigated have input for F10.7 (or a similar index in the case of DTM2013). Therefore, any changes to F10.7 generally led to appropriate changes in the predicted mass density.

Currents in the ionosphere and magnetosphere are enhanced from the injection of charged particles from the solar wind, leading to variations in the magnetic field measured at Earth's surface. This can occur when the magnetic field of the Earth and solar wind are anti-parallel. The Ap index is based on magnetometer data on Earth and is a proxy for the amount of geomagnetic activity in the Earth's ionosphere / magnetosphere. Increased activity is usually caused by coronal mass ejections (during solar maximum) or high-speed solar wind from coronal holes (during solar minimum) interacting with the Earth's magnetosphere leading to "geomagnetic storms". Due to coupling of atmospheric layers, this increase in energy can also affect the temperature of regions where LEO satellites orbit.

Solar X-ray radiation, although much higher in energy than UV light has a much lower average flux and therefore less of an effect on the atmospheric density. However, short bursts of X-ray radiation from solar flares can momentarily increase this flux by orders of magnitude from the background value. Table 3 lists the average background flux and the average number of daily C- and M-class flares (or flares of flux $10^{-6}\,\mathrm{W\,m^{-2}}$ to $10^{-5}\,\mathrm{W\,m^{-2}}$ and $10^{-5}\,\mathrm{W\,m^{-2}}$ to $10^{-4}\,\mathrm{W\,m^{-2}}$, respectively) across the 10-day periods.

Five AMD models, i.e., MSISE90, MSISE00, JB2008, DTM2013 and the SERC model, and no-drag model are assessed via comparing one-day OP results with COSMIC precise ephemerides. The 3D distance error of the final epoch of the day is saved, as well as the in-track error of the final epoch and the maximum in-track distance error during the whole day. The average of these values over each 10-day window is plotted along with samples, shown in Fig. 5 for 2014–2015 and Fig. 6 for 2018–2019, respectively. For some specific C_d and C_r values, it happens that some AMD models fail to output the effective density values at some epochs during the day. As a result, these samples are removed for comparison.

The final epoch 3D distance errors in 2018–2019 are smaller than those in 2014–2015 due to less mass density interaction with satellites in the solar minimum period. For example, the average one-day OP errors over last ten days in 2018–2019 present up to 45 m for no-drag model, while those in 2014–2015 come to approximately 160 m. For each 10-day window of each AMD model, the final epoch 3D distance errors are stable with respect to different C_d samples. For example, the standard deviation (STD) values for the 3D distance errors over forty days during 2018–2019 are 0.434m, 0.539m, 0.555m, 0.680m, 0.619m, 0.670m for no-drag, MSISE90, MSISE00, JB2008, DTM2013 and the SERC model, respectively, while those values for the 2014–2015 period are 0.706m, 1.145m, 0.932m, 2.024m, 0.860m, 0.818m. Hence, it illustrates that the C_d value is not the major factor that affects drag calculation for COSMIC satellites, and Monte Carlo simulations using the reference mean and STD values for C_d are able to quantify the uncertainty associated with C_d.

For the period of 2014–2015 (solar maximum) in Fig. 5, the results of AMD models tend to be grouped together and yield significant improvement in terms of the one-day OP performance compared to no-drag calculation. DTM2013 generates extremely small final epoch 3D distance errors for the first and last ten days, presenting mean val-

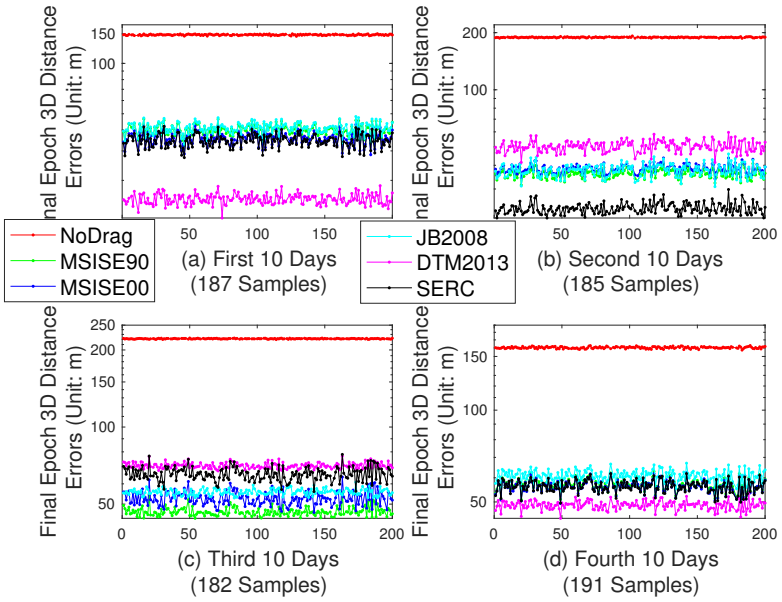

Figure 5: Final epoch 3D distance errors over days for 2014–2015. Subfigure (a) - (d) show average final epoch 3D distance errors of each 10 days for all available samples, respectively. OP results without drag calculation are represented by red curves; MSISE90 OP results are represented by green curves; MSISE00 OP results are represented by blue curves; JB2008 OP results are represented by cyan curves; DTM2013 OP results are represented by pink curves; SERC OP results are represented by black curves.

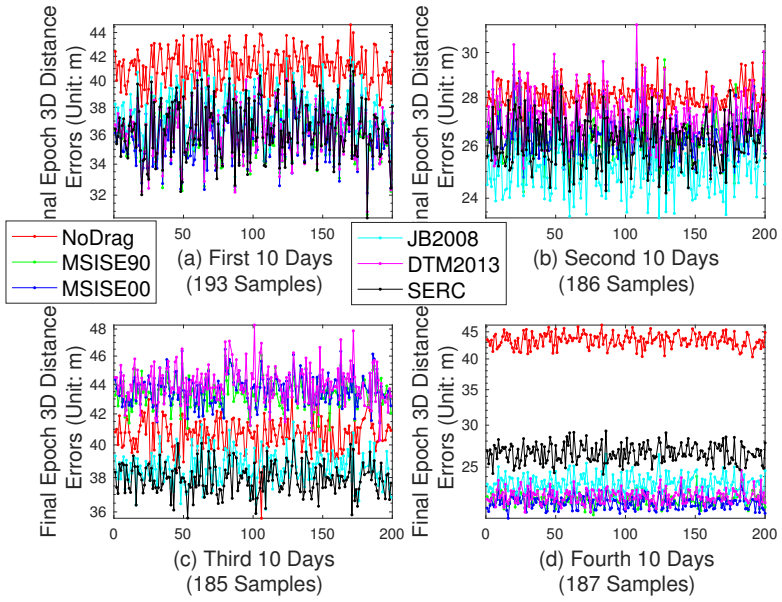

Figure 6: Final epoch 3D distance errors over days for 2018–2019.

ues of around 20 m with respect to all samples. The SERC model shows the smallest er-

rors for the second ten days, and also outperforms other models except DTM2013 for the first and last ten days. Surprisingly, for the third ten days, MSISE90 is slightly better than MSISE00 and presents the smallest 3D distance error for the final epoch.

For the period of 2018–2019 (solar minimum) shown in Fig. 6, only for the last ten days, AMD models yield obvious improvement in terms of the 3D distance error for the final epoch compared to no-drag calculation in OP. For the other thirty days, OP performance without drag is very close to that with AMD models. Surprisingly, for the third ten days, the OP result without drag is even better than that with MSISE90/00 and DTM2013 models. The SERC model generates the smallest 3D distance errors. Except for the third ten day period, all AMD models improve the OP performance by reducing the 3D distance errors at the final epoch over the no-drag case.

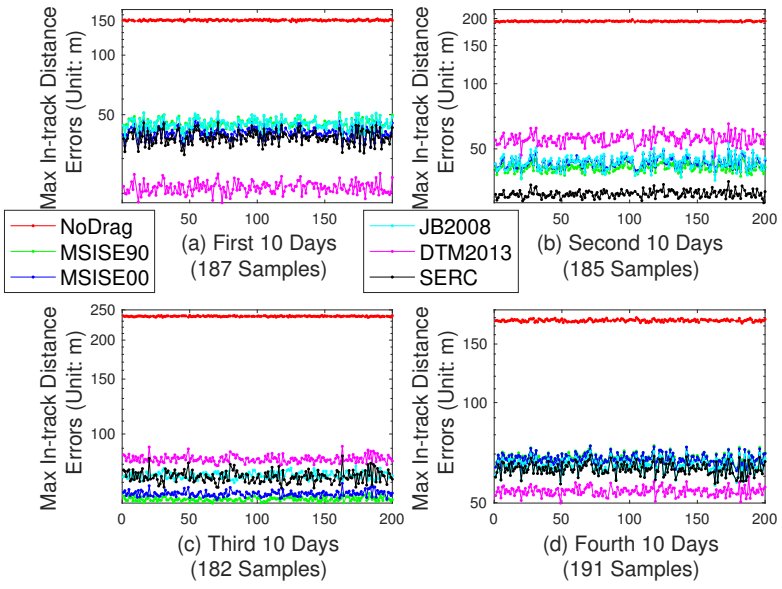

Figure 7: Maximum in-track distance errors over days for 2014–2015.

The results for different AMD models in terms of the maximum in-track distance during the day are also plotted, see Figs. 7 and 8. They have similar tendencies as the 3D distance errors, but with slightly different magnitudes. It reveals the dominating contribution of the density uncertainty to the in-track position. Also worth noting is that the maximum in-track distance errors can be larger than the final epoch 3D distance errors presented in Figs. 5 and 6, which indicates the largest deviations between OP and reference orbits may not occur at the final epoch.

The average errors over all C_d/C_r samples are shown for each day in Figs. 9 and 10, for the periods of 2014–2015 and 2018–2019, respectively. In-track errors at the final epoch are presented in the bottom subfigure instead of the maximum in-track distance errors that resemble the 3D distance errors as explained above. These values present different patterns compared to the 3D distance errors in the top subfigure due to non-positive values generated by AMD models for some days. It should be mentioned all errors are calculated by subtracting OP results from the reference ephemerides. It is shown that no-drag case always yields positive in-track errors in Fig. 9, which indicates that OP without accounting for drag perturbation always results in leading positions in the in-track direction. This is consistent with the fact of drag effect.

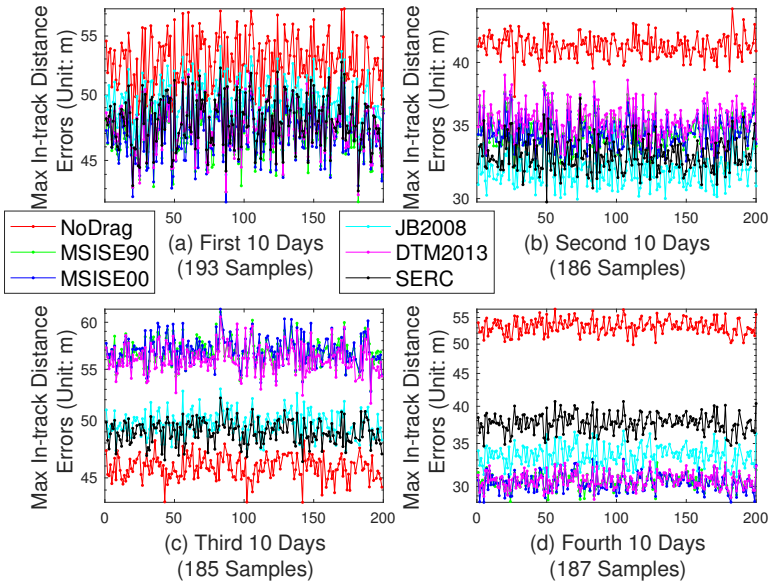

Figure 8: Maximum in-track distance errors over days for 2018–2019.

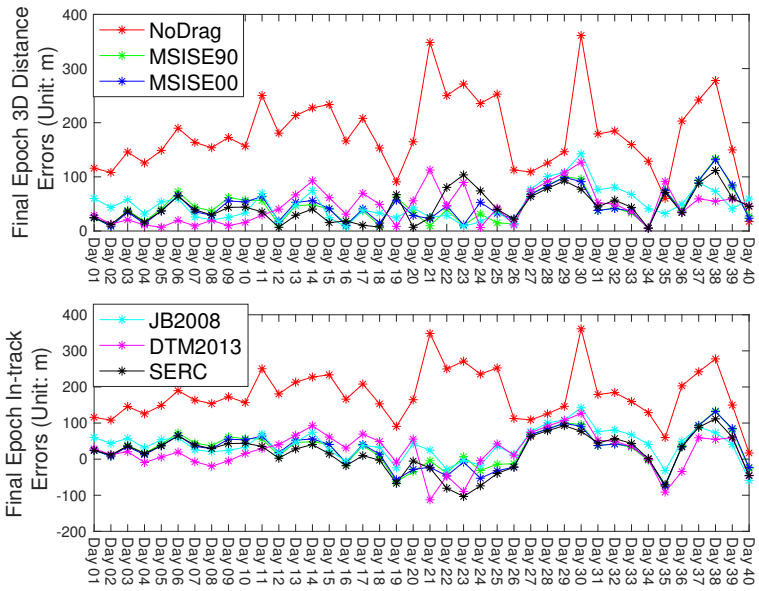

Figure 9: Average final epoch in-track errors over samples for 2014–2015. The top subfigure shows average final epoch in-track errors for all days. OP results without drag calculation are represented by red curves; MSISE90 OP results are represented by green curves; MSISE00 OP results are represented by blue curves; JB2008 OP results are represented by cyan curves; DTM2013 OP results are represented by pink curves; SERC OP results are represented by black curves.

However, the no-drag in-track error is not always positive during 2018–2019, as seen in Fig. 10. It changes between positive and negative values. Interestingly all the AMD

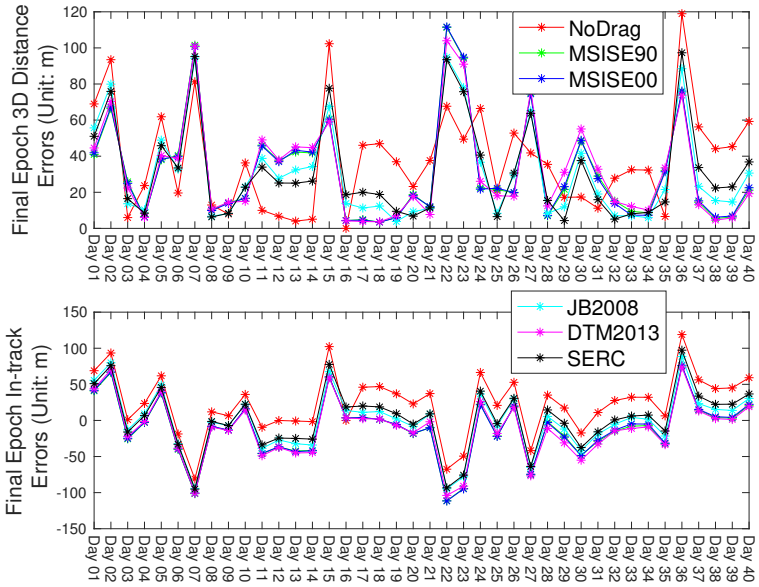

Figure 10: Average final epoch in-track errors over samples for 2018–2019.

models also share a very similar trend as the no-drag case, following it almost exactly for all testing days for final epoch in-track error (bottom subfigure of Fig. 10). The no-drag in-track error remains the most positive compared to the AMD models in all days but one. However, because the 3D error is the absolute distance to the zero point (the reference ephemerides), this means that on days where all models (and no-drag) have negative in-track error, the no-drag case actually has the lowest 3D error. This would suggest the AMD models do worse than the no-drag case as evidenced in the top subfigure of Fig. 10. However, this is unlikely to be true especially as the no-drag case counter-intuitively has a negative in-track error.

The small difference between no-drag and the AMD models in-track error on any given day would suggest that there is very little effect from atmospheric drag on the satellite's orbit; little atmospheric drag is expected during solar minimum, so this is reasonable. However, the seemingly random trend of positive and negative in-track errors across the forty days also suggests there is some contributing factor not taken into account. Some unmodelled or dismodelled perturbations, for example, an imperfect SRP model may lead to OP discrepancy in the in-track direction.

For the period of 2014–2015 (solar maximum) in Fig. 9, AMD models significantly improve the OP performance compared to no-drag calculation. The last twenty days have larger variations in terms of both the 3D distance errors and the in-track errors at the final epoch than the first twenty days. For example, two peak values for the no-drag case occur on Day 21 and Day 30 for no-drag calculation. Referring to Fig. 4 and Table 3 we can gain some insight into why this may be the case. UV flux (represented here through F10.7) does not suggest a very large atmospheric drag effect should be seen on these peak days, at least compared to the first 7 days. Day 30 has a reasonably high flux at 185 but Day 21 is on the low end compared to the first 10 days at 168 - the highest occurs on Day 7 at 201. The daily background X-ray flux is also similar for the first ten days compared to days 21 and 30, at or just under $10^{-6}\,\mathrm{W\,m^{-2}}$.

Table 4: Statistics of 3D distance errors of OP for forty days (on average of samples) during 2014–2015 (unit: m).

	Mean Value	STD Value	RMS Value
No-Drag	179.653	70.171	192.552
MSISE90	45.035	29.843	53.819
MSISE00	45.897	28.478	53.826
JB2008	48.943	29.463	56.936
DTM2013	46.400	32.791	56.580
SERC	45.107	28.430	53.129

However, day 21 and 30 both fall within the third-ten-days window, where the average number of C-class solar flares was 7.7 per day, the highest of any 10-day period investigated, while 0.6 M-class flares per day is the second highest after the second-ten-days window. Specifically, Day 21 has 10 C-class flares and Day 30 has 12, well above the average. However there were no M-class flares for either day. This differs significantly with the first ten days which have no more than 5 C-class flares on any given day. Secondly, the daily Ap index is much higher during the last 20 days compared to the first 20 days, and especially more than the first 8 days when F10.7 is highest. On Day 21 the daily Ap index is 11, higher than the maximum Ap index on any of the first 8 days. Day 30 with a daily Ap index of 6 is actually similar to the index of the first 8 days, however this comes off a relatively high daily index of 18 on the previous day - Day 29.

Therefore, as expected the daily F10.7 flux plays a significant role in predicting the effect of atmospheric drag (as evidenced by the discrepancy in the no-drag case), but the other space weather factors also play a role in explaining large discrepancies. A combination of relatively high F10.7, relatively large number of C-class flares (in other words increased X-ray flux), and relatively high activity in the Earth's magnetosphere/ionosphere (evidenced through the Ap index) seem to come together to create the largest peaks in 3D errors. There are other days in which these factors individually are higher but not in combination.

The large variation in 3D error for the final 20 days are probably also the result of swings in the values of F10.7, background X-ray flux and the Ap index. The Ap index in particular has large variation in the daily and maximum recorded indices, especially for the last 10 days. The first 20 days in comparison are much lower in absolute value generally, and with no massive variation from one day to the next. As the days in the chosen 10-day windows are not always consecutive, it is important to keep in mind that a peak in the error from one day to the next may in fact be much more gradual than seen in Figs. 9 and 10.

The statistical values, i.e., mean, STD, Root Mean Square (RMS), of each ten days in terms of the final epoch 3D distance errors are shown in Figs. 11 and 12 for the two time periods of solar maximum and solar minimum, respectively. These three statistical values are also provided for all forty days in terms of the final epoch 3D distance errors are in Tables 4 and 5 for the two time periods.

From Table 4, it is seen that the mean value of no-drag case is approximately 4 times of that of other AMD models during the solar maximum period. Its STD value is also the largest. Two MSISE models share similar statistical values, the mean and RMS values of MSISE90 are even smaller than that of MSISE00. JB2008 yields the worst per-

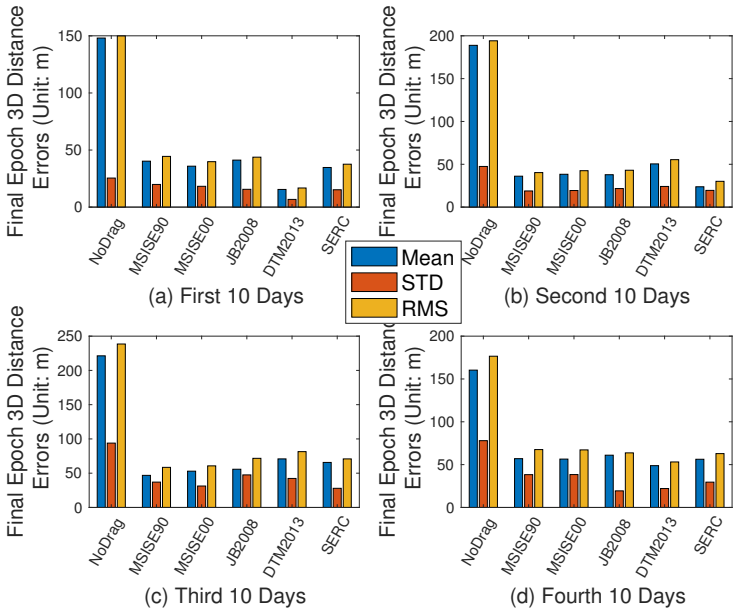

Figure 11: Statistics of final epoch 3D distance errors for 2014–2015. Subfigure (a) - (d) show statistical values, i.e., mean, STD and RMS, of final epoch 3D distance errors of each 10 days using different AMD models. Mean values are represented by blue bars; STD values are represented by brown bars; RMS values are represented by yellow bars.

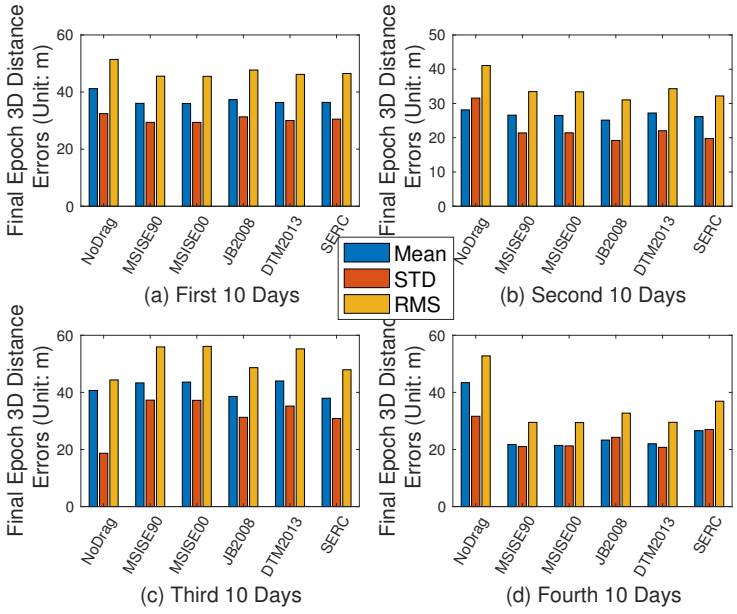

Figure 12: Statistics of final epoch 3D distance errors for 2018–2019.

formance while the SERC model generates the smallest RMS values and STD values among all AMD models for the chosen days, except that its mean value is only slightly larger than MSISE90. Hence it can be concluded the SERC model outperforms other models

Table 5: Statistics of 3D distance errors of OP for forty days (on average of samples) during 2018–2019 (unit: m).

	Mean Value	STD Value	RMS Value
No-Drag	38.355	28.655	47.662
MSISE90	31.921	28.272	42.407
MSISE00	31.879	28.356	42.429
JB2008	31.086	26.864	40.865
DTM2013	32.392	27.900	42.523
SERC	31.771	26.891	41.406

in OP during this solar maximum period. From Table 5, all three statistical values for OP with all AMD models and without drag calculation are close. AMD models does not reduce OP errors significantly compared to no-drag modeling during the solar minimum period, generating only about 5 m to 7 m smaller RMS values. Two MSISE models share similar performance with DTM2013. JB2008 presents the best OP performance among all AMD models, slightly better than the SERC model, with a 0.6 m smaller RMS value during this solar minimum period.

6 Conclusion

This paper introduces a newly developed empirical atmospheric mass density model, dubbed the SERC model. To assess its performance, a new data source of COSMIC satellite reference ephemerides was used to compare the orbit prediction performance using the SERC model and four other existing empirical AMD models for aerodynamic drag calculation. The calculation of OP without drag was also carried out. Two time periods of forty days, representing the solar maximum and minimum conditions, respectively, were chosen to conduct OP. Results were compared to precise reference ephemerides and analyzed using relevant space weather indices. The lack of the COSMIC satellites' drag data within any of the AMD models tested here ensured that we are carrying out an unbiased test. This is an important point, as many previous comparative analyses of AMD models have an unfair advantage for more recent models - the same data used to create the new models are also used to test its performance against older models (Picone et al., 2002; Bruinsma, 2015).

Accounting for the ion contribution at higher atmospheric altitudes (e.g., around 800 km) based on the IRI 2016 model, the SERC model does improve the atmospheric density calculation, and consequently improves the OP performance. During the solar maximum period, the SERC model generates better OP results compared to all other state-of-the-art AMD models. During the solar minimum period, the SERC model yields slightly worse results than JB2008 but outperforms other AMD models.

7 Acknowledgement

The authors would like to acknowledge the support of the Cooperative Research Centre for Space Environment Management (SERC Limited) through the Australian Governments Cooperative Research Centre Program. Space weather data for the F10.7 index used in this paper are the observed flux values from the Penticon observatory, British Columbia, Canada in sfu or solar flux units, and retrieved for this study from the daily NOAA reports on solar activity (`https://www.swpc.noaa.gov/products/report-and`

-forecast-solar-and-geophysical-activity and https://www.spaceweather.gc.ca/solarflux/sx-5-flux-en.php). The Ap index values were determined from the Kp values obtained from the GFZ Helmholtz Centre Potsdam (https://www.gfz-potsdam.de/en/kp-index/). The X-ray data was obtained from https://www.spaceweatherlive.com/en/solar-activity/solar-flares which ultimately has its origin in the GOES-15 satellite and the NOAA website https://www.swpc.noaa.gov/products/goes-x-ray-flux.

References

Akmaev, R. A. (2011). Whole atmosphere modeling: Connecting terrestrial and space weather. *Reviews of Geophysics*, *49*(4). doi: 10.1029/2011RG000364

Altadill, D., Magdaleno, S., Torta, J., & Blanch, E. (2013). Global empirical models of the density peak height and of the equivalent scale height for quiet conditions. *Advances in Space Research*, *52*(10), 1756 - 1769. doi: https://doi.org/10.1016/j.asr.2012.11.018

Bilitza, D. (2018). IRI the international standard for the ionosphere. *Advances in Radio Science*, *16*, 1–11. doi: 10.5194/ars-16-1-2018

Bilitza, D., Altadill, D., Truhlik, V., Shubin, V., Galkin, I., Reinisch, B., & Huang, X. (2017). International reference ionosphere 2016: From ionospheric climate to real-time weather predictions. *Space Weather*, *15*(2), 418-429. doi: 10.1002/2016SW001593

Bowman, B. R., Tobiska, W. K., & Marcos, F. A. (2006). A new empirical thermospheric density model JB2006 using new solar indices. In *AIAA/AAS astrodynamics specialist conference, AIAA* (p. 6166). doi: 10.2514/6.2006-6166

Bowman, B. R., Tobiska, W. K., Marcos, F. A., Huang, C. Y., Lin, C. S., & Burke, W. J. (2008). A new empirical thermospheric density model JB2008 using new solar and geomagnetic indices. In *AIAA/AAS astrodynamics specialist conference and exhibit* (p. 6438). doi: 10.2514/6.2008-6438

Bruinsma, S. (2015). The DTM-2013 thermosphere model. *Journal of Space Weather and Space Climate*, *5*, A1. doi: 10.1051/swsc/2015001

Bruinsma, Sean, Arnold, Daniel, Jggi, Adrian, & Snchez-Ortiz, Noelia. (2017). Semi-empirical thermosphere model evaluation at low altitude with GOCE densities. *J. Space Weather Space Clim.*, *7*, A4. doi: 10.1051/swsc/2017003

Calabia, A., & Jin, S. (2016). New modes and mechanisms of thermospheric mass density variations from GRACE accelerometers. *Journal of Geophysical Research: Space Physics*, *121*(11), 11–191.

Doornbos, E., Den Ijssel, J. V., Luehr, H., Foerster, M., & Koppenwallner, G. (2010). Neutral density and crosswind determination from arbitrarily oriented multiaxis accelerometers on satellites. *Journal of Spacecraft and Rockets*, *47*(4), 580–589.

Emmert, J. (2015). Thermospheric mass density: A review. *Advances in Space Research*, *56*(5), 773–824.

Folkner, W. M., Williams, J. G., Boggs, D. H., Park, R. S., & Kuchynka, P. (2014). The planetary and lunar ephemerides DE430 and DE431. *Interplanetary Network Progress Report*, *196*, 1–81.

Fong, C., Yang, S., Chu, C., Huang, C., Yeh, J., Lin, C., ... Chi, S. (2008, Nov). FORMOSAT-3/COSMIC constellation spacecraft system performance: After one year in orbit. *IEEE Transactions on Geoscience and Remote Sensing*, *46*(11), 3380-3394. doi: 10.1109/TGRS.2008.2005203

Hairer, E., & Wanner, G. (1999). Stiff differential equations solved by radau methods. *Journal of Computational and Applied Mathematics*, *111*(1-2), 93–111.

He, C., Yang, Y., Carter, B., Kerr, E., Wu, S., Deleflie, F., ... Norman, R. (2018). Review and comparison of empirical thermospheric mass density models. *Progress*

in Aerospace Sciences, *103*, 31 - 51. doi: https://doi.org/10.1016/j.paerosci.2018.10.003

Hedin, A. E. (1983). A revised thermospheric model based on mass spectrometer and incoherent scatter data: MSIS-83. *Journal of Geophysical Research: Space Physics*, *88*(A12), 10170–10188. doi: 10.1029/JA088iA12p10170

Hedin, A. E. (1987). MSIS-86 thermospheric model. *Journal of Geophysical Research: Space Physics*, *92*(A5), 4649–4662. doi: 10.1029/JA092iA05p04649

Hedin, A. E. (1991). Extension of the MSIS thermosphere model into the middle and lower atmosphere. *Journal of Geophysical Research-Space Physics*, *96*(A2), 1159–1172. doi: 10.1029/90JA02125

Hwang, C., Lin, T., Tseng, T., & Chao, B. F. (2008, Nov). Modeling Orbit Dynamics of FORMOSAT-3/COSMIC Satellites for Recovery of Temporal Gravity Variations. *IEEE Transactions on Geoscience and Remote Sensing*, *46*(11), 3412-3423. doi: 10.1109/TGRS.2008.2004789

Hwang, C., Tseng, T.-P., Lin, T., Švehla, D., & Schreiner, B. (2009, May). Precise orbit determination for the FORMOSAT-3/COSMIC satellite mission using GPS. *Journal of Geodesy*, *83*(5), 477–489. doi: 10.1007/s00190-008-0256-3

Jacchia, L. G. (1965, Jan). Static Diffusion Models of the Upper Atmosphere with Empirical Temperature Profiles. *Smithsonian Contributions to Astrophysics*, *8*, 215.

Jacchia, L. G. (1970, May). New Static Models of the Thermosphere and Exosphere with Empirical Temperature Profiles. *SAO Special Report*, *313*.

Jacchia, L. G. (1971, May). Revised Static Models of the Thermosphere and Exosphere with Empirical Temperature Profiles. *SAO Special Report*, *332*.

Jacchia, L. G. (1977, Mar). Thermospheric Temperature, Density, and Composition: New Models. *SAO Special Report*, *375*.

Jones, W., & Obitts, D. (1970). *Global representation of annual and solar cycle variation of foF2 monthly median 1954-1958*. Institute for Telecommunication Sciences.

Liu, H., Lühr, H., Henize, V., & Köhler, W. (2005). Global distribution of the thermospheric total mass density derived from CHAMP. *Journal of Geophysical Research: Space Physics*, *110*(A4).

Liu, H.-L., Foster, B. T., Hagan, M. E., McInerney, J. M., Maute, A., Qian, L., ... Oberheide, J. (2010). Thermosphere extension of the whole atmosphere community climate model. *Journal of Geophysical Research: Space Physics*, *115*(A12). doi: 10.1029/2010JA015586

March, G., Doornbos, E., & Visser, P. (2019). High-fidelity geometry models for improving the consistency of CHAMP, GRACE, GOCE and Swarm thermospheric density data sets. *Advances in Space Research*, *63*(1), 213 - 238. doi: https://doi.org/10.1016/j.asr.2018.07.009

Mehta, P. M., Walker, A. C., Sutton, E. K., & Godinez, H. C. (2017). New density estimates derived using accelerometers on board the CHAMP and GRACE satellites. *Space Weather*, *15*(4), 558–576.

Montenbruck, O., & Gill, E. (2000). *Satellite orbits: models, methods, and applications*. Springer.

Nicolet, M. (1961, Sep). Density of the Heterosphere Related to Temperature. *SAO Special Report*, *75*.

Oyekola, O. (2019). Comparison of IRI-2016 model-predictions of F2-layer peak density height options with the ionosonde-derived hmF2 at the equatorial station during different phases of solar cycle. *Advances in Space Research*, *64*(10), 2064 - 2076. doi: https://doi.org/10.1016/j.asr.2019.04.022

Panzetta, F., Bloßfeld, M., Erdogan, E., Rudenko, S., Schmidt, M., & Müller, H. (2019, Mar 01). Towards thermospheric density estimation from slr observations of leo satellites: a case study with ande-pollux satellite. *Journal of Geodesy*, *93*(3),

603 353–368. doi: 10.1007/s00190-018-1165-8
604 Picone, J. M., Hedin, A. E., Drob, D. P., & Aikin, A. C. (2002). NRLMSISE-00
605 empirical model of the atmosphere: Statistical comparisons and scientific issues.
606 *Journal of Geophysical Research: Space Physics*, *107*(A12), SIA 15-1-SIA 15-16.
607 doi: 10.1029/2002JA009430
608 Qian, L., Burns, A. G., Emery, B. A., Foster, B., Lu, G., Maute, A., ... Wang, W.
609 (2014). The ncar tie-gcm. In *Modeling the ionospherethermosphere system* (p. 73-
610 83). American Geophysical Union (AGU). doi: 10.1002/9781118704417.ch7
611 Qian, L., & Solomon, S. C. (2012, Jun 01). Thermospheric density: An overview of
612 temporal and spatial variations. *Space Science Reviews*, *168*(1), 147–173. doi: 10
613 .1007/s11214-011-9810-z
614 Ries, J., Bettadpur, S., Eanes, R., Kang, Z., Ko, U., McCullough, C., ... Tapley,
615 B. (2016). Development and evaluation of the global gravity model GGM05.
616 *CSR-16-02, Center for Space Research, The University of Texas at Austin*.
617 Rush, C., Fox, M., Bilitza, D., Davies, K., McNamara, L., Stewart, F., & PoKempner,
618 M. (1989). Ionospheric mapping: An update of foF2 coefficients. *Telecommunication journal*, *56*(3), 179-182.
619
620 Shubin, V. (2015). Global median model of the F2-layer peak height based on ionos-
621 pheric radio-occultation and ground-based digisonde observations. *Advances in*
622 *Space Research*, *56*(5), 916 - 928. doi: https://doi.org/10.1016/j.asr.2015.05.029
623 Siemes, C., de Teixeira da Encarnação, J., Doornbos, E., van den IJssel, J., Kraus,
624 J., Pereštý, R., ... Holmdahl Olsen, P. E. (2016). Swarm accelerometer data pro-
625 cessing from raw accelerations to thermospheric neutral densities. *Earth, Planets*
626 *and Space*, *68*(1), 92. doi: 10.1186/s40623-016-0474-5
627 Simões, P. J., Hudson, H. S., & Fletcher, L. (2015). Soft X-ray pulsations in solar
628 flares. *Solar Physics*, *290*(12), 3625–3639.
629 Sutton, E. K., Nerem, R. S., & Forbes, J. M. (2007). Density and winds in the
630 thermosphere deduced from accelerometer data. *Journal of Spacecraft and Rock-*
631 *ets*, *44*(6), 1210-1219. doi: 10.2514/1.28641
632 Vallado, D. A. (2001). *Fundamentals of astrodynamics and applications*. Springer
633 Science & Business Media.